Lawrence Berkeley National Laboratory
Recent Work

Title

Ion acceleration in laser generated megatesla magnetic vortex

Permalink

Journal

ISSN

Authors

Park, J
Bulanov, SS
Bin, J
et al.

Publication Date

DOI

Peer reviewed

Ion Acceleration in Laser Generated Mega Tesla Magnetic Vortex

J. Park,[1] S. S. Bulanov,[1, a)] J. Bin,[1] Q. Ji,[1] S. Steinke,[1] J.-L. Vay,[1] C. G.R. Geddes,[1] C. B. Schroeder,[1] W. P. Leemans,[1, b)] T. Schenkel,[1] and E. Esarey[1]

Lawrence Berkeley National Laboratory, Berkeley, California 94720, USA

Magnetic Vortex Acceleration (MVA) from near critical density targets is one of the promising schemes of laser-driven ion acceleration. 3D particle-in-cell simulations are used to explore a more extensive laser-target parameter space than previously reported on in the literature as well as to study the laser pulse coupling to the target, the structure of the fields, and the properties of the accelerated ion beam in the MVA scheme. The efficiency of acceleration depends on the coupling of the laser energy to the self-generated channel in the target. The accelerated proton beams demonstrate high level of collimation with achromatic angular divergence, and carry a significant amount of charge. For PW-class lasers, this acceleration regime provides favorable scaling of maximum ion energy with laser power for optimized interaction parameters. The mega Tesla-level magnetic fields generated by the laser-driven co-axial plasma structure in the target are prerequisite for accelerating protons to the energy of several hundred MeV.

I. INTRODUCTION

Laser-based ion acceleration (see[1–4] and references cited therein) has received considerable attention over the last two decades for the potential applications to diverse research areas: fundamental particle physics, inertial confinement fusion, warm-dense matter, medical therapy, etc. It is expected that with the fast development of multi-PW laser facilities[5–11] laser ion acceleration will be able to generate ion beams with energies in excess of 100 MeV, required by many applications. Up to now laser systems were only able to achieve the acceleration of ions with energies approaching 100 MeV[12–14]. While most of the experimental results were obtained in the Target Normal Sheath Acceleration (TNSA) regime[15–18], higher ion energies are expected to be generated by employing advanced regimes of laser ion acceleration, as it was demonstrated in Refs.[12,14], as well as different targets ranging from nm-scale solid density foils to near critical density (NCD) slabs, gas jets, and liquid jets. These regimes include, to name a few, Radiation Pressure Acceleration (RPA)[19–21], Shockwave Acceleration (SWA)[22], Relativistic Transparency (RIT)[23], and Magnetic Vortex Acceleration[24]. Analytical and computer simulation estimates show that a PW or several PW laser system may be able to generate ions with energies ranging from several hundred MeV to GeV per nucleon in these regimes (see[25] and references cited therein). We note that NCD targets as well as composite targets with NCD parts attracted a lot of attention recently not only to be used for ion acceleration[21,35], but also for brilliant gamma-ray and electron-positron pair production[36–39]. All these results rely on the physics of intense laser pulse interaction with NCD plasma, the basics of which are best illustrated by the MVA.

In this paper we study the MVA regime for a PW-class laser system. This regime uses NCD slabs as targets, in contrast to thin micron or sub-micron solid density foils used in other regimes. Experimental studies of such targets have reported maximum ion energy of several tens of MeV per nucleon

at sub-PW laser systems[26–29] and previous 2D/3D computer simulation studies showed that the maximum ion energy can reach GeV level with PW-class laser systems[30–34].

In the MVA scheme, an intense laser beam can penetrate the NCD target and expels the electrons by the ponderomotive force. It thereby creates a low density channel in the electron plasma component along the laser propagation axis. The waveguide model[30] successfully describes the properties of the laser field inside the channel flow and we use it to maximize the proton energy. In the waveguide with the cylindrical geometry, the magnetic field is described by the TE mode ($E_z = 0$), $H_z = A J_1(\kappa r)\cos(\omega t - kz)$, where J_1 is the Bessel function of the first kind and $\kappa = 1.84/R_{ch}$; R_{ch} is the radius of the channel, ω and k are the laser angular frequency and the wave vector, respectively. The dimensionless vector potential inside the waveguide is expressed as[32]

$$a_{ch} = \left(\frac{2}{K} \frac{P}{P_c} \frac{n_e}{n_{cr}} \right)^{1/3}, \qquad (1)$$

where $K = 1/13.5$ is the geometrical factor, P is the laser power, $P_c = 2m_e^2 c^5/e^2 = 17 \text{GW}$ is a characteristic power for relativistic self-focusing[41], n_e is the electron density, and $n_{cr} = m_e \omega^2/(4\pi e^2)$ is the plasma critical density; e and m_e are the charge and mass of an electron respectively, and c is the speed of light in vacuum. The radius of the channel is determined from balancing the energy gain of an electron in laser field and the field of an ion column, $R_{ch} = \lambda (n_e/n_{cr})^{1/2} a_{ch}^{1/2}/2^{30}$. Using Eq.(1), we obtain the radius of the channel in terms of the laser pulse power[32]

$$R_{ch} = \frac{\lambda}{\pi} \left(\frac{n_{cr}}{n_e} \right)^{1/3} \left(\frac{2}{K} \frac{P}{P_c} \right)^{1/6}. \qquad (2)$$

The maximum achievable ion energy in the MVA scheme is determined by several parameters such as target density, target length, laser power, laser focal spot size, etc. The optimum condition is basically obtained by equating the laser energy inside the channel, W_p, to the total electron energy, W_e, acquired after interacting with the laser: $W_p = W_e$, where $W_p = \pi R_{ch}^2 \tau a_{ch}^2 m_e c n_{cr} K$ and $W_e = \pi R^2 L_{ch} n_e a_{ch} m_e c^2$. Here, we assumed that the electron acquires the energy, $m_e c^2 a_{ch}$, on

average, which is validated by the PIC simulation results[30]. Using Eqs.(1-2), and the condition, $W_p = W_e$, we finally get the optimum condition:

$$\frac{n_e}{n_{cr}} = 2^{1/2} K \left(\frac{P}{P_c} \right)^{1/2} \left(\frac{L_p}{L_{ch}} \right)^{3/2}, \qquad (3)$$

where $L_p = c\tau$ is the laser pulse length, τ is the laser pulse duration (the full width at $1/e$ of the amplitude of the electric field). We will use Eq.(3) to determine our simulation parameters.

As the laser propagates in the self-generated channel, it accelerates electrons in its wake. These electrons form a thin filament along the central axis carrying a strong electric current, which is due to the plasma lensing effect[40]. The radius of the electron beam is determined from the balance of the transverse electric field of the ion column $E_i = 2\pi e n_i R_{ch}$ and the self field of an electron beam, $E_e = 2\pi e (n_e \gamma_e) R_b$. From the condition $E_i = E_e$, we obtain $R_b = R_{ch}/\gamma_e$, where γ_e is the Lorentz factor of the bulk of electrons accelerated forward[32], obtained from the condition that the electron velocity is equal to the group velocity of an EM pulse in a waveguide of radius R_{ch}, $\gamma_e = (\sqrt{2}/1.84)(2P/KP_c)^{1/6}(n_{cr}/n_e)^{1/3}$. Thus, a co-axial plasma structure is formed with the current flowing along the axis and the return current flowing in the channel wall, resulting in a strong azimuthal magnetic field confined inside the channel.

The magnetic field strength at $r = R_b$ is approximated as $B_{ch} \approx E_e = 2\pi e n_e R_{ch} \gamma_e^2$ [32]. Using Eq.(2), we see that the magnetic field strength in the channel scales with the laser pulse power as

$$B_{ch} = 2\pi e \left(\frac{\lambda}{\pi} \right) n_{cr} \left(\frac{\sqrt{2}}{1.84} \right)^2 \left(\frac{2}{K} \frac{P}{P_c} \right)^{1/2}. \qquad (4)$$

(We note that a similar approach to generating strong azimuthal magnetic fields in plasma was reported in Refs.[42–44], where a long laser pulse was interacting with a pre-filled channel.) When the laser, followed by this pinched current, exits the target from the back, the magnetic field begins to expand in the transverse direction. In doing so, the field displaces the electron component of the plasma with respect to the ion one, and, as a result, both strong longitudinal and transverse electric fields are generated, which accelerate and collimate ions in the form of a well defined beam with achromatic divergence. These accelerated ions mainly originate from the same filamentary structure, since the electron current pre-accelerates a number of ions as it propagates through the ion channel.

Most previous studies of the MVA scheme have been done through 2D Particle-in-Cell (PIC) simulations that successfully qualitatively explained how the mechanism works although it was understood that the magnetic vortex is in a 3D structure[24,30,31]. So, in order to get quantitatively accurate results on the MVA scheme, 3D PIC simulations are required. Recent 3D simulations of the MVA scheme[29,33,34] explored ion acceleration for different laser powers and polarization (linear and circular cases), but left the study of the coupling and field structure out.

In this paper, we explore the MVA scheme using 3D PIC simulations in a more extensive parameter space: we vary the laser power, the laser focal spot size, target density, and pulse duration. Here, we focus on the study of laser pulse coupling to the target, the structure of the fields in the target, as the laser propagates through it, the scaling of the maximum ion energy with laser parameters, such as power and duration, as well as on the properties of the accelerated ion beam, which is of great importance for applications and beam transport.

We show that the intense laser interaction with an NCD target creates a co-axial plasma current structure, which generates a localized mega Tesla-level magnetic field. The converging electric field behind the rear-surface of the target makes a contribution to the collimation of the ion beam and therefore the accelerated ions reveal achromatic divergence in the angular distribution. Moreover a favorable scaling of maximum ion energy is revealed when two conditions are satisfied: (i) the laser focal spot size matches the radius of the self-generated channel in Eq.(2) and (ii) the target density and the length are determined by the optimum condition in Eq.(3).

The rest of the paper is organized as follows. The simulation setup and the parameter space are described in Section II. The simulation results are in Section III and IV. The summary and conclusion are in Section V.

II. 3D PIC SIMULATION SETUP

We use the 3D relativistic full particle-in-cell (PIC) code WarpX[45]. The target is an NCD-hydrogen plasma with $n_e = 0.69 - 4.52 \, n_{crit}$, with longitudinal thickness of $L_{ch} = 32 \mu m$. The target density is uniform in the range of $5\mu m < z < 37\mu m$ and is zero elsewhere.

The laser pulse has both transverse and longitudinal Gaussian profile and propagates along the z-axis. It is tightly focused at the target front surface, $z = 5\mu m$, with the focal spot size (laser waist), $w_0 = 1.488 - 3.0\mu m$ (half-width at $1/e^2$ of the intensity peak). The laser wavelength is $\lambda = 0.8\mu m$. A virtual laser antenna is used to inject the laser and is located within the simulation domain at $z = 1\mu m$. The electric field is linearly polarized along the x-axis. The laser intensity is $I = 6.3 - 56 \times 10^{21} W/cm^2$ and the corresponding dimensionless vector potential is $a_0 \equiv eE_0/m_e \omega c = 54 - 161$. The laser pulse duration is chosen to be $\tau = 13.5, 27,$ and 54 fs (defined as the full width at $1/e$ of the amplitude of the electric field). The laser power is $P = 0.22 - 1.96$PW and the total laser energy is $E_L = 4.9 - 87.8$J. We note that experiments reported on in Refs.[12,14] had approximately 0.3 PW of laser power on target, thus, the laser power range covered in our simulations connects well with what is available at high power laser facilities worldwide. It also provides an idea how the maximum ion energy in the MVA regime will scale with the increase of laser power, which is scheduled to happen at different laser facilities (see Refs.[5–11]).

Table I shows parameter sets of our 3D simulations organized into five groups. Each group has a different focal spot size from $w_0 = 1.49$ to $3\mu m$. The laser pulse duration is $\tau = 27$ fs in groups I–III, 13.5 fs in group IV, and 54fs in

Run	a_0	τ (fs)	n_e/n_{crit}	$w_0(\mu\text{m})$	P(PW)	$E_L(J)$	$E_{i,\text{max}}$(MeV)
I-1	161	27	4.52	1.49	1.96	43.9	466
I-2	118	27	3.32	1.49	1.05	23.6	283
I-3	91	27	2.56	1.49	0.63	14.0	182
I-4	70	27	1.96	1.49	0.37	8.3	132
I-5	54	27	1.51	1.49	0.22	4.9	83
II-1	120	27	4.52	2.0	1.96	43.9	360
II-2	88	27	3.32	2.0	1.05	23.6	196
II-3	68	27	2.56	2.0	0.63	14.0	153
II-4	52	27	1.96	2.0	0.37	8.3	108
III-1	80	27	4.52	3.0	1.96	43.9	138
III-2	58	27	3.32	3.0	1.05	23.6	107
III-3	45	27	2.56	3.0	0.63	14.0	85
III-4	35	27	1.96	3.0	0.37	8.3	50
IV-1	114	13.5	1.60	2.1	1.96	21.9	227
IV-2	84	13.5	1.17	2.1	1.05	11.8	140
IV-3	65	13.5	0.91	2.1	0.63	7.0	89
IV-4	49	13.5	0.69	2.1	0.37	4.2	55
V-1	161	54	4.52	1.49	1.96	87.8	412
V-2	118	54	3.32	1.49	1.05	47.2	275
V-3	91	54	2.56	1.49	0.63	28.0	196
V-4	70	54	1.96	1.49	0.37	16.6	131

TABLE I. Initial parameters of 3D simulations organized into five groups; a_0: dimensionless vector potential, τ: laser pulse duration, n_e: electron density, w_0: laser waist, P: laser power, E_L: laser energy, and $E_{i,\text{max}}$: maximum ion kinetic energy. Each group has a different laser spot size w_0. The laser power varies from 0.22 to 1.96 PW. The electron density is chosen by the optimum condition in Eq.(3), except in group V. The spot sizes from groups I, IV, and V match the channel radius in Eq.(2).

group V. The target densities in each group are chosen by the optimum condition in Eq.(3) except in group V. Group V has the same parameters as group I except for the pulse duration. The laser spot sizes from group I, IV, and V match the channel radius in Eq.(2), that is, $w_0 = R_{\text{ch}}$, while groups II and III have larger focal spot sizes, $w_0 > R_{\text{ch}}$. The maximum ion energy is listed in the table and will be discussed in the next section.

The simulation domain size is $(L_x, L_y, L_z) = (60\mu\text{m}, 60\mu\text{m}, 80\mu\text{m})$ and the number of cells is $(N_x, N_y, N_z) = (512, 512, 2400)$. The cell sizes are $dz = 0.0417\lambda$ ($= 0.3 - 0.55c/\omega_{\text{pe}}$) and $dx = dy = 0.144\lambda$ ($= 1 - 2c/\omega_{\text{pe}}$), where λ is the laser wavelength, $\omega_{\text{pe}} = (4\pi n_e e^2/m_e)^{1/2}$ is the electron plasma frequency.

The boundary conditions are periodic along the transverse directions and open along the longitudinal direction (z-axis) with a perfectly matched layer (PML) that absorbs outgoing waves very efficiently[46]. The simulation runs until 400 fs (4000 time iterations) at which the ion energy is fully saturated. We used 1 particle/cell/species and the simulation results converged at higher resolutions up to $N_x = 2400$ and $N_z = 4800$.

Throughout this paper, we largely discuss the simulation result of Run I-2 in Table I, otherwise we specify the simulation parameters.

III. LASER PULSE PROPAGATION IN NCD PLASMA

As was mentioned above, the laser pulse makes a channel both in the electron and ion components of the plasma, as it propagates through the target, see Fig 1(a-b), where the results of Run-I for n_e and n_i distributions are shown at $t = 226$ fs. Here $a_0 = 118$, $\tau = 27$ fs, and $P = 1.05$ PW. The propagation of the laser inside this channel is accompanied by the generation of a strong azimuthal magnetic field (Fig. 1c) and longitudinal electric field, as the laser exits the channel (Fig. 1d). Note that inside the channel, there is a pinched filamentary structure along the central axis at $x = y = 0$. The filament is not perfectly straight along the central axis but wiggles along the x-axis as the electrons oscillate with the laser field. The filament carries the electric current toward the $-z$ direction, dominated by faster electrons, which induces the azimuthal magnetic field [Fig.1(c)]. As the magnetic field exits the target, it displaces the surface electrons and a strong electric field $E \sim 10 - 60\text{TV/m}$ is induced over the distance of $\sim 10\mu\text{m}$ behind the rear surface of the target [Fig.1(d)].

In order to visualize the structure of the current and magnetic field in the channel, we show in Fig. 1(e) a 3D image of the ion density distribution. The magnetic field (blue ribbon) is circulating around the filamentary structure along the central axis inside the low-density channel. The cloud near the surface of the target represents the accelerated ions.

Now, we compare the formation of the channel for different laser focal sizes. Figure 2 shows the electron density distribution (top), the current density J_z (center), and the magnetic field strength B_x (bottom) before the laser pulse exits the target ($t = 144$ fs), for different laser focal spot sizes, $w_0 = 1.49\mu\text{m}$ (left: Run I-2), $2.0\mu\text{m}$ (middle: Run II-2), and $3.0\mu\text{m}$ (right: Run III-2). These variables are plotted in the $y - z$ slice plane to address the azimuthal component of the magnetic field B_ϕ, which is B_x in the $y - z$ plane, distinguished from the laser field. Here, the laser power and the energy are fixed as $P = 1.05\text{PW}$ and $E_L = 23.6J$ in the three runs. Only the left column panel shows that the laser spot size matches the channel radius in Eq.(2), $w_0 = R_{\text{ch}}$, while the other runs have $w_0 > R_{\text{ch}}$. The radius of the trailing channel expands as time goes by. As the laser spot size becomes larger, the laser pulse is dispersed and loses the energy sideways as seen in the right column panel. As a result, the current density of the filament along the central axis and the induced magnetic field become weaker for $w_0 > R_{\text{ch}}$. The ion energy will be lowered for the larger spot sizes. Note that the strongest magnetic field is localized inside the leading channel and reaches around 0.4MT (the left column panel), while the magnetic field in the trailing channel is reduced by one order of magnitude. As for $w_0 < R_{\text{ch}}$ (not shown in the figure), the laser pulse would develop filamentation which prevents efficient channel generation as discussed in[32].

Figure 3 shows the channel structure in more detail in the $x - y$ slice cut on $z = 28\mu\text{m}$ at $t = 144$fs (Fig. 2 left column). The channel is surrounded by thin dense walls about twice higher than the background density [Fig. 3(a and c)] and the high density bump at $x = y = 0$ is the plasma pinch which carries the electric current.
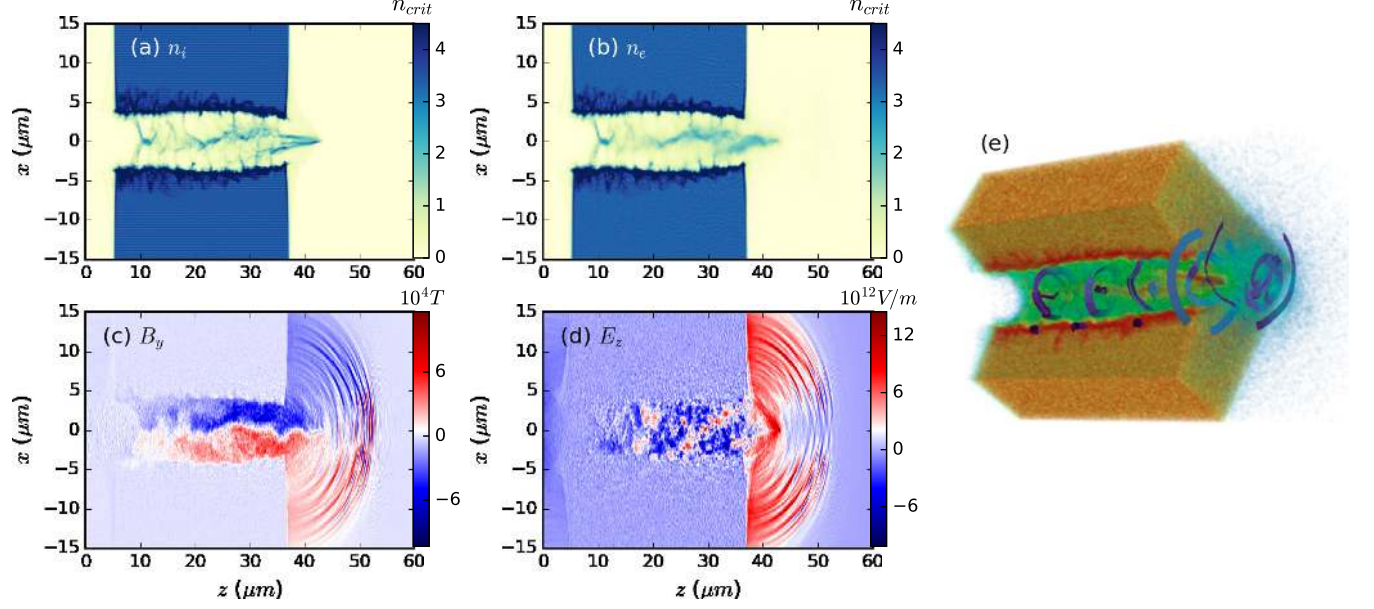
FIG. 1. Simulation result (Run I-2 in Table I) around the acceleration stage at $t = 226$ fs: (a) ion density n_i/n_{crit}, (b) electron density n_e/n_{crit}, (c) B_y field, and (d) E_z field, in the $x-z$ slice at $y = 0$. (e) 3D image of the ion density distribution; a strong magnetic field (ribbon) inside the low-density channel is generated.
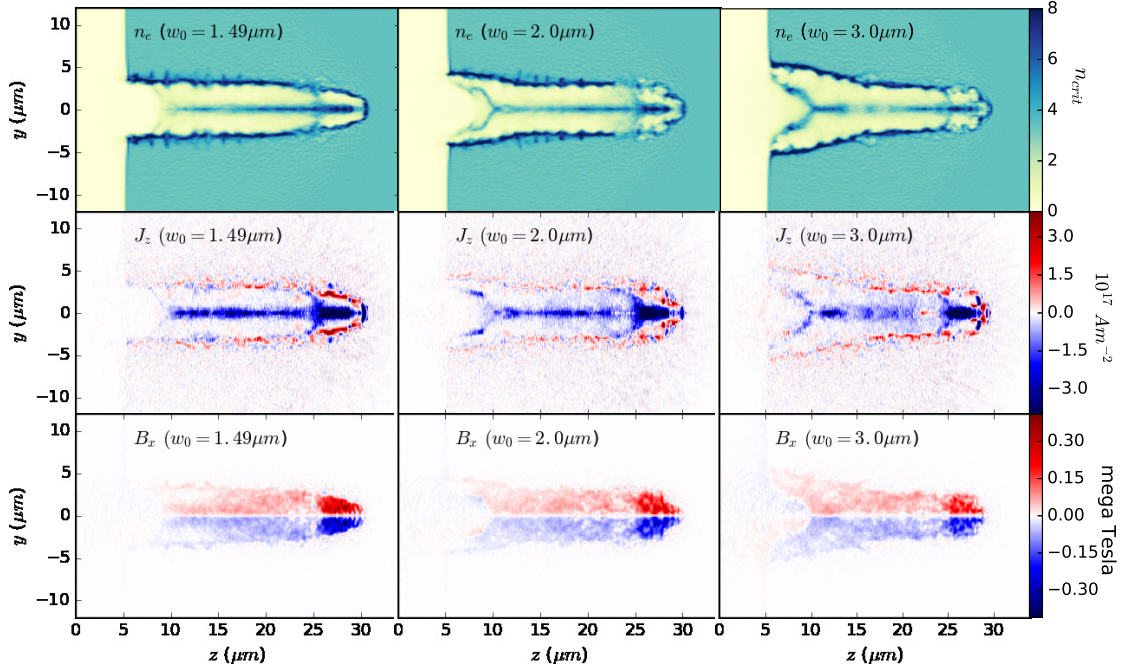

FIG. 2. (from top to bottom) 2D slice $y-z$ cut of the electron density (n_e), the current density J_z, and the magnetic field B_x for different laser focal spot sizes, $w_0 = 1.49\mu$m (left: Run I-2), 2.0μm (middle: Run II-2), and 3.0μm (right: Run III-2), before the laser pulse exits the target $(t = 144\text{fs})$. In the left column panel, the laser spot size matches the leading channel radius, $w_0 = R_{ch}$ while the other runs have $w_0 > R_{ch}$.
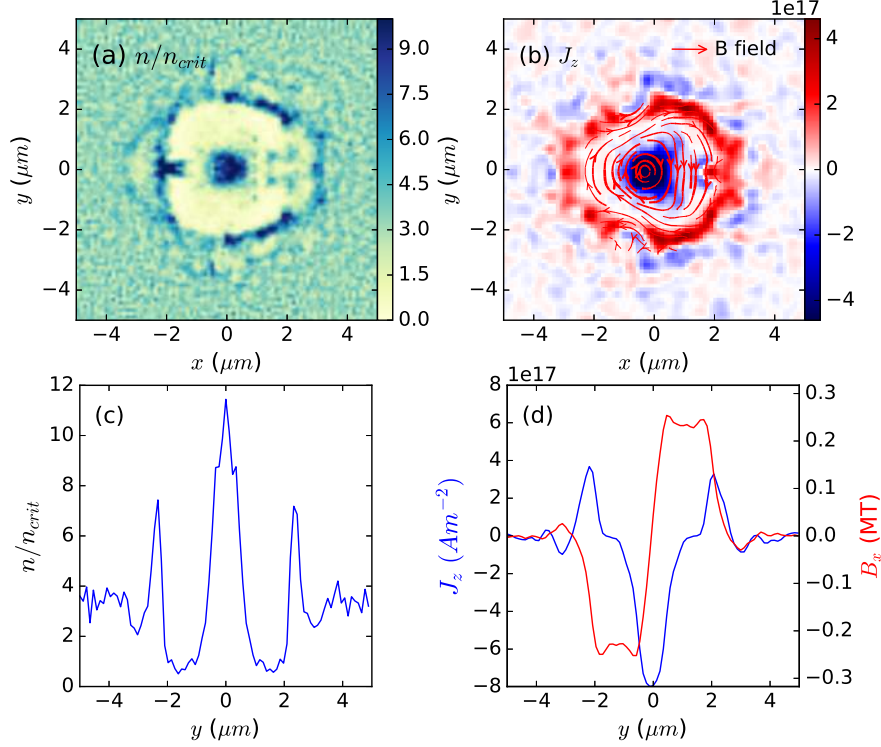
FIG. 3. Channel structure (Run I-2) at $t = 144$fs: (a) electron density n_e/n_{crit}, (b) electric current density J_z with the B field lines (red) in the $x - y$ slice cut on $z = 28\mu$m, (c) 1D electron density profile, and (d) 1D electric current density J_z (blue) and B_x field (red) profiles along the y-axis at $x = 0$.

Figure 3(b) shows co-axial structure of the current density J_z. The peak value of the current density is $J_z = 8 \times 10^{17}$ I/m^2 along the $-z$ direction and is compensated by the return current flowing in the walls of the channel, thereby perfectly screening the magnetic field outside the channel (see also Fig. 3(d)). Inside the channel, the magnetic field lines (red) are circulating around the plasma pinch with a peak value of $B \sim 0.25$ mega Tesla as seen in Fig. 3(b and d).

The intense laser interaction with an NCD target creates a co-axial plasma current structure, which generates a localized mega Tesla-level magnetic field in the leading channel. A strong magnetic field is obtained when the laser focal size matches the channel radius, which affects ion acceleration as we will see in the next section.

IV. ION ACCELERATION

In this section, we explore the properties of the accelerated ion beam for several different parameters. Figure 4 shows the ion energy distribution (top) and the charge density (bottom) at three consecutive time steps during the acceleration stage $t = 185 - 226$ fs in the $x - z$ plane ($y = 0$). In Fig. 4(a-c), the ions pinched by the electrons in a thin filament are accelerated at the rear-edge of the target (the energy is in logarithmic color-scales). The magenta line is the longitudinal electric field E_z along the central axis. During this stage, the E_z field strength decreases from 60 to 10 TV/m and the ion energy increases from 30 to 220 MeV. In Fig. 4(d-f), the charge density $\rho_e = e(n_i - n_e)$ around the rear-surface of the target is plotted, overlaid with the electric field lines (black), $\mathbf{E} = E_x \hat{x} + E_z \hat{z}$. As the magnetic vortex inside the channel exits the target, it expands transversely and displaces the surface electrons. Therefore the rear-surface of the target is positively charged while the negative charge is concentrated on the apex of the filament with fast moving electrons along the central axis. The electric field lines emitting from the rear-surface converge onto the apex of the filament. Furthermore, the relativistic electrons of the filament strengthen the transverse component of the electric field due to relativistic effects. Their velocity can be characterized by the group velocity of the laser pulse inside the channel, or in terms of *gamma*-factor, $\gamma_e = (\sqrt{2}/1.84)(2P/KP_c)^{1/6}(n_{cr}/n_e)^{1/332}$. The converging electric field indeed makes a contribution to the collimation of ions.

Figure 5(a) shows the transverse momentum $p_x - p_y$ distribution of the ions at several energy levels centered at $E = 50, 96, 143, 190$, and 236 MeV (Run I-2). The distribution reveals highly collimated accelerated ions. The influence of laser power on the divergence of the ion beam is examined,
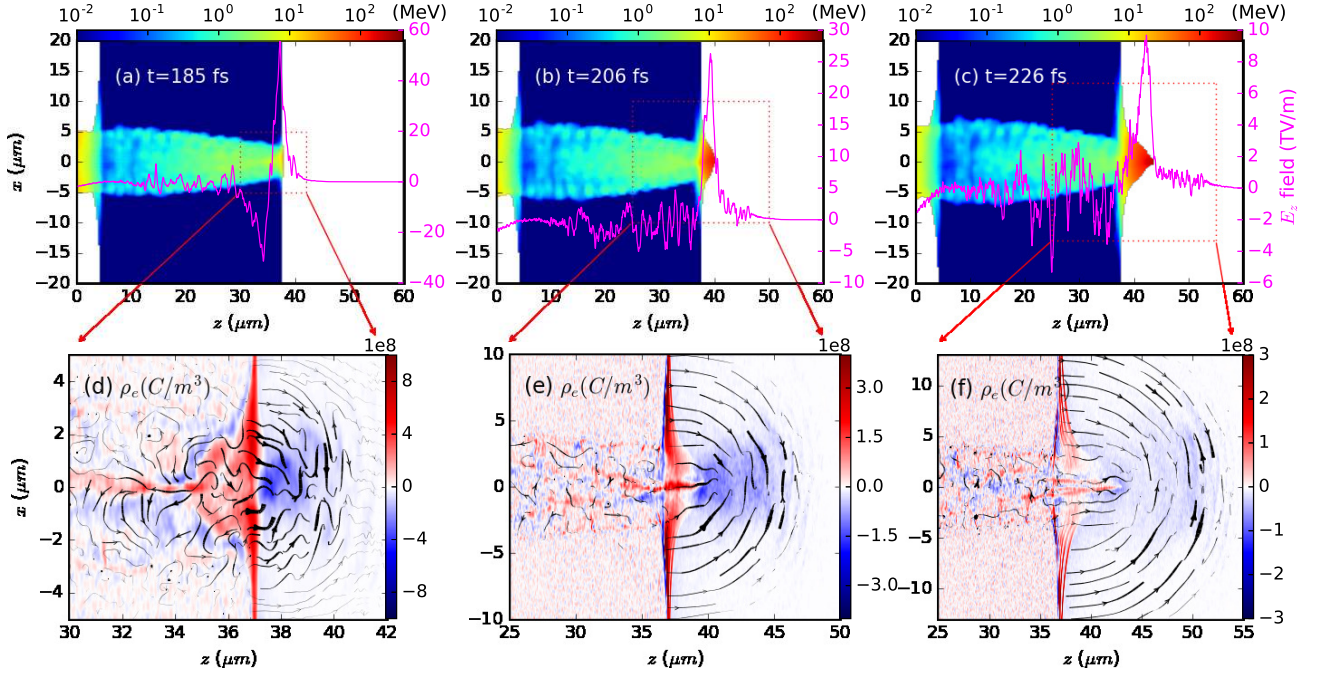
FIG. 4. Three consecutive time steps (Run I-2) during the acceleration stage $t = 185$, 206, and 226 fs: (a-c) ion energy distribution in the $x-z$ plane ($y = 0$) (logarithmic color scales represent the energy in MeV) and the E_z field along the central axis $x = y = 0$ (magenta). (d-f) charge density $\rho_e = e(n_i - n_e)$ and the electric field lines (black) $\mathbf{E} = E_x\hat{x} + E_z\hat{z}$ in the $x-z$ plane ($y = 0$).

as shown in Fig. 5(b) (Run I-1 to I-4); the divergence is defined as $2\Delta\theta = 2(\langle\theta^2\rangle - \langle\theta\rangle^2)$, where $\langle\ \rangle$ is the average of the angular distribution in each energy bin, $\theta = \cos^{-1}[p_z/p]$, and p_z is the z-component moment. The energy is normalized by the maximum ion energy in each run. The divergence $2\Delta\theta$ is around 5 to 8 degrees between $0.3 < EE_{i,max} < 0.8$ for the laser powers, $0.35 < P(PW) < 1.96$. All the runs reveal achromatic divergence. The converging electric field behind the rear surface of the target makes a contribution to such an achromatic divergence of the ion beam. Such a narrow angular dispersion is not commonly found in other acceleration schemes. Exceptionally, a recent experiment on TNSA with a large laser focal diameter $2w_0 \sim 100\lambda$ performed at the peta-watt BELLA laser facility revealed an achromatic divergence with $2\Delta\theta = 100\text{mrad} = 5.7°$ of the ion beam[47]. In Fig. 4(f), the histogram shows the number of the accelerated ions in each energy bin with the size of $\Delta E = 13\text{MeV}$, and about 5×10^{10} (2×10^{10}) ions are accelerated above $E = 50$ (100) MeV. The spectrum reveals quite a broad energy spectrum. From the particle tracking method (not shown in the figure), we found that energetic protons originate from the edge of the ion filament. In addition, as the initial positions of the protons are located farther from the rear-surface, they gain higher energy. The broadness of the energy spectrum results from the summation of the energy spectra at different locations. We measure that 18% (or 20%) of the laser energy is transferred to the total ions, and 3.3% (or 4.4%) is transferred to the ions above $E = 50$ MeV for P=1PW of Run I-2 (or P=2PW of Run I-1). More than 50% of the laser energy is used to heat the electrons for both cases.

Figure 6 shows time evolution of the maximum ion energy for different laser powers (Run I-1 to I-4). Here, the peak of the laser pulse arrives at the front surface at $t = 53\text{fs}$. The ions start to be accelerated around $t = 180\text{fs}$ after the laser pulse exits the target at $t = 170\text{fs}$. The ion gains about 80% of the maximum energy during the acceleration stage from $t = 180$ fs to 240fs, and reaches saturation at $t > 300$ fs. The accelerated ions come from the edge of the filament when the channel in the ion distribution opens at the rear side of the target, which lags behind the channel in the electron distribution.

Figure 7 (top) shows the maximum ion energy vs. the laser power from Run I-1 to I-5 ($\tau = 27\text{fs}$), IV-1 to IV-4 ($\tau = 13.5\text{fs}$), and V-1 to V-4 ($\tau = 54\text{fs}$) in Table I. Interestingly, the data points fit to a power-law, $E_{i,max} \propto P^\sigma$, and the power-law index is $\sigma \sim 0.8$. This scaling can be explained in the framework of a simple analytical model. We assume that the ions are accelerated by a pulsed longitudinal electric field E, which is $E = B_{max}$, and the length of this field is R_{ch}. We also assume that this field moves with the speed of light. Then for the ions, we can write the equation of motion:

$$dp/dt = \varepsilon(x - ct) = \varepsilon(\psi),\tag{5}$$

where p is the ion momentum, $\psi = x - ct$, and $\varepsilon(\psi)$ is the normalized electric field E. Equation (5) leads to

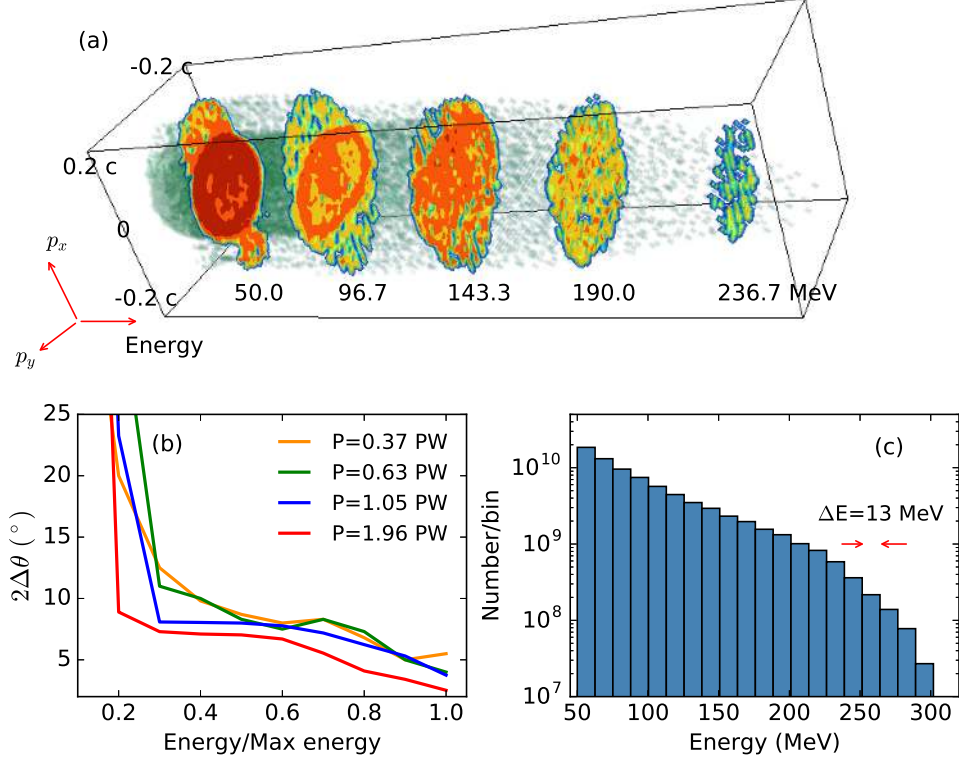$$mc^2\frac{d\tilde{p}}{d\psi}\left[\frac{\tilde{p}}{\sqrt{1+\tilde{p}^2}} - 1\right] = \varepsilon(\psi),\tag{6}$$

FIG. 5. (a) Transverse momentum $p_x - p_y$ distribution of the ions at several energy levels centered at $E = 50, 96, 143, 190$, and 236 MeV (Run I-2). (b) Divergence vs. normalized energy in the ion energy-angular distribution, for different laser powers (Run I-1 to I-4). The energy is normalized by the maximum energy in each run. (c) The number of the accelerated ions in each energy bin with the bin size $\Delta E = 13$MeV (Run I-2).

where $\tilde{p} = p/m_i c$ is the dimensionless momentum. The integration of Eq. (6) over ψ becomes

$$F \equiv \int_0^{R_{ch}} \varepsilon(\psi) d\psi = mc^2 \left[\sqrt{1 + \tilde{p}^2} - \tilde{p} - 1 \right]. \quad (7)$$

We solve Eq.(7) for the gamma factor $\gamma = \sqrt{1 + \tilde{p}^2}$ and get

$$\gamma = \frac{(2 + 2f + f^2)}{2(1 + f)}, \quad (8)$$

where $f = F/m_i c^2$. Here, we assume that ε is constant over the phase interval $(0, R_{ch})$, and is equal to zero elsewhere. Using the scalings, $R_{ch} \sim P^{1/6}$ in Eq.(2) and $E_{ch} \sim B_{ch} \sim P^{1/2}$ in Eq.(4), we get $f \sim P^{2/3}$. Then, the solution in Eq.(8) gives a scaling of

$$\gamma = \begin{cases} 1 + f^2/2 & \text{for } f \ll 1 \\ f/2 & \text{for } f \gg 1 \end{cases} \quad (9)$$

$$E_{i,max} \sim \begin{cases} P^{4/3} & \text{for } f \ll 1 \\ P^{2/3} & \text{for } f \gg 1 \end{cases} \quad (10)$$

For the laser-plasma interaction parameters considered in this paper, the maximum ion energy ranges from 50 MeV to 500

MeV, or $1.05 < \gamma < 1.5$. In this energy range the difference between the solution, given by Eq. (8), and the $P^{0.8}$ scaling, obtained from the 3D PIC simulations, is less than 5%. Thus, there is a good agreement between a simple analytical model and simulations results.

In Fig. 7 (top), the maximum ion energy for the short pulse $\tau = 13.5$fs (green dot) is reduced 50% compared to that of $\tau = 27$fs (blue dot) for a given laser power because the total laser energy is a half. Interestingly, the maximum ion energy (red x) for the longest pulse duration $\tau = 54$fs is comparable to that of $\tau = 27$fs. Note that the parameters for the longest pulse do not meet the optimum condition in Eq.(3). To meet the optimum condition, either the density n_e or the target length L_{ch} needs to be twice. For $\tau = 54$fs, the residual part of the laser pulse longer than 27fs escapes the target through the channel without heating the electrons inside, which is confirmed by the simulation (not shown in figures). Therefore, the maximum ion energy for a given laser power is similar between the two pulses, $\tau = 27$fs and 54fs. If the parameters for the pulse duration $\tau = 54$fs meet the optimum condition in Eq.(3), we predict that the maximum ion energy will increase significantly.

Figure 7 (bottom) shows the maximum magnetic field generated inside the channel vs. the laser power from Run I-1 to
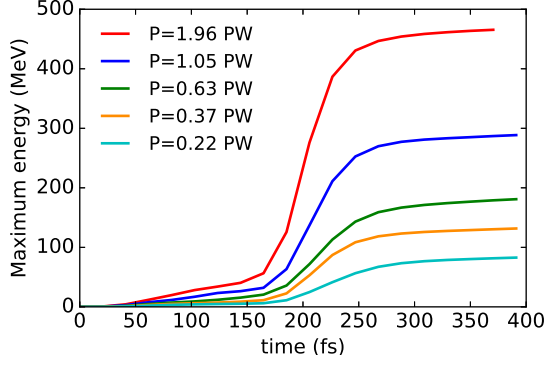
FIG. 6. Maximum ion energy as a function of time for different laser powers (Run I-1 to I-5).

I-5 ($\tau = 27$fs). The maximum field strength is localized inside the leading edge of the channel, $B \sim 0.4$MT (or 0.6MT) for the laser power $P = 1$PW (or 2PW). The power-law scaling $B_{max} \propto P^{0.55}$ is close to the theoretical prediction where the power-law index is given by $1/2$ in Eq.(4).

In this section, the ion beams revealed high level of collimation and achromatic angular divergence due to the converging electric field behind the target. Such a significant amount of charge $\sim 10^{10} H^+$ above 100MeV for $P \sim 1$PW makes the MVA scheme potentially a desirable source for the application to hadron therapy. A favorable energy-power scaling $E_{i,max} \propto P^{0.8}$ is obtained from the 3D PIC simulations, and is also predicted from our simple analytic models as long as the optimum conditions, Eq.(2) and (3), are satisfied.

V. SUMMARY AND CONCLUSIONS

We studied laser driven ion acceleration in the MVA regime by employing 3D PIC simulations and analytic models. In order to optimize the process of acceleration from the point of view of increasing maximum ion energy we studied the coupling of the laser pulse to the target by a comprehensive parameter scan. We varied the focal spot size, the power, and the duration of the laser, as well as the density of the target.

We showed that the optimal acceleration happens when two conditions are satisfied. First, the laser is focused at the front of the target to a spot, which radius is equal to (or not greater than) the radius of the laser-generated channel in the target, and, second, the density and thickness of the target are given by the laser depletion condition.

The 3D computer simulations revealed the structure of the electric and magnetic fields inside the target, as well as that of the plasma itself. It was shown that the laser creates a co-axial plasma structure in the target along the direction of its propagation: a laser-generated channel with high density wall and a strong pinched electron current, flowing along the channel central axis. A strong magnetic field is created by the electric current flowing in the filament and the return current, flowing in the wall. The co-axial structure of the currents ensures that
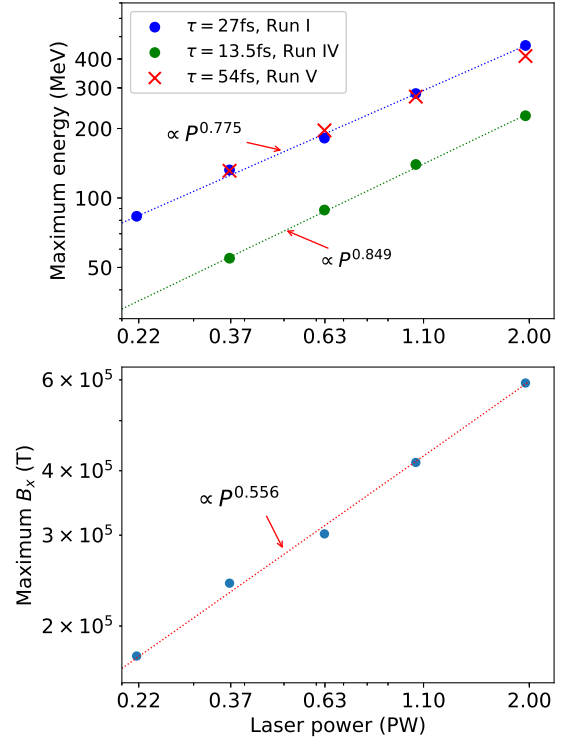

FIG. 7. (Top) Maximum ion energy vs. laser power for $\tau = 27$fs (Run I-1 to I-5), $\tau = 13.5$fs (Run IV-1 to IV-4), and $\tau = 54$fs (Run V-1 to V-4). The power-law scaling is $\propto P^{0.775}$ for $\tau = 27$fs (blue dashed) and $\propto P^{0.849}$ $\tau = 13.5$fs (green dashed). (Bottom) Maximum azimuthal B field inside the channel vs. laser power for $\tau = 27$fs (Run I-1 to I-5). The power-law scaling is $\propto P^{0.55}$.

the magnetic field is localized inside the channel. Due to the strong pinching of the central filament, which is due to the fact that the electrons have relativistic energies, the magnetic field amplitude can almost reach MT-level (6×10^5 Tesla observed in a simulation for Run I-1, a 2 PW case), which is in good agreement with analytical estimates[32].

We showed that as the intense laser-driven electron current and magnetic field leave the target from its back, strong longitudinal and transverse electric fields are established. These fields accelerate the protons to several hundred MeV maximum energy and collimate them into a well defined beam with achromatic angular divergence with $2\Delta\theta \sim 7^o$.

The 3D PIC simulation results prove the validity of the waveguide analytical model of the MVA regime proposed in Refs[30,32]. Using this model we were able to analyze the scaling of the magnetic field in the channel, which scales as the square root of laser power, and the scaling of the maximum ion energy, which scales as (laser power)$^{0.8}$ for laser pulse power ranging from 0.2 PW to 2 PW. We note that the scaling is obtained, assuming the optimal coupling of the laser to the target.

We note that the Gaussian temporal and spatial profiles used to model the laser pulse in 3D PIC simulations result in higher fraction of laser energy localized inside the focal spot than it

is usually achieved in experiments. In Table I we considered several cases of laser pulse focusing and showed that the case $w_0 = R_{ch}$ (which corresponds to the optimal laser energy coupling to the self-generated plasma channel) produces higher energy ions than the cases with $w_0 > R_{ch}$. The maximum ion energy decrease can be approximately estimated as the ratio of laser power inside the $r < R_{ch}$ spot to the power of 0.8, according to the scaling found from 3D PIC simulation results. This results in approximately 20% maximum ion energy reduction when going from $w_0 = 1.5 \ \mu m$ to $w_0 = 2.0 \ \mu m$ spot size. If the laser pulse is focused in a way that a smaller than in the Gaussian case portion of total energy is localized inside the focal spot, than we can estimate the reduction in maximum ion energy using the same arguments as above. For example, let us assume that a 1 PW laser pulse is focused on an NCD target so that only 50% of its energy is confined in the focal spot. In this case the laser power coupled to the plasma channel is $\sim$500 TW, instead of $\sim$900 TW in the pure Gaussian case, which would result in 40% smaller maximum ion energy.

The above mentioned considerations along with the obtained energy-power scaling might serve as a guideline for future experiments at PW-class laser facilities.

[1] G. Mourou, T. Tajima, and S. V. Bulanov, Rev. Mod. Phys. **78**, 309 (2006).

[2] H. Daido, M. Nishiuchi, and A. S. Pirozhkov, Reports on Progress in Physics **75**, 056401 (2012).

[3] A. Macchi, M. Borghesi, and M. Passoni, Rev. Mod. Phys. **85**, 751 (2013).

[4] S. V. Bulanov, Ja. J. Wilkens, T. Zh. Esirkepov, G. Korn, G. Kraft, S. Kraft, M. Molls, and V. S. Khoroshkov, Phys. Usp. **57**, 1149 (2014).

[5] K. Nakamura, H. S. Mao, A. J. Gonsalves, H. Vincenti, D. E. Mittelberger, J. Daniels, A. Magana, C. Toth, and W. P. Leemans, IEEE Journal of Quantum Electronics **53**, 1 (2017).

[6] S. Gales, K. A. Tanaka, D. L. Balabanski, F. Negoita, D. Stutman, O. Tesileanu, C. A. Ur, D. Ursescu, I. Andrei, S. Ataman, M. O. Cernaianu, L. DAlessi, I. Dancus, B. Diaconescu, N. Djourelov, D. Filipescu, P. Ghenuche, D. G. Ghita, C. Matei, K. Seto, M. Zeng, and N. V. Zamfir, Rep. Prog. Phys. **81**, 094301 (2018).

[7] ELI-beamlines, https://www.eli-beams.eu/.

[8] CORELS, https://www.ibs.re.kr/eng/sub02_03_05.do.

[9] XCELS, http://www.xcels.iapras.ru

[10] VULCAN, https://www.clf.stfc.ac.uk/Pages/Vulcan-2020.aspx.

[11] C. Danson, D. Hillier, N. Hopps, and D. Neely, High Power Laser Science and Engineering **3**, e3 (2015).

[12] I. J. Kim, K. H. Pae, C. M. Kim, C.-L. Lee, I. W. Choi, H. T. Kim, H. Singhal, J. H. Sung, S. K. Lee, H. W. Lee, P. V. Nickles, T. M. Jeong, and C. H. Nam, Phys. Plasmas **23**, 070701 (2016).

[13] F. Wagner, O. Deppert, C. Brabetz, P. Fiala, A. KleinSchmidt, P. Poth, V. A. Schanz, A. Tebartz, B. Zielbauer, M. Roth, et al., Phys. Rev. Lett. **116**, 205002 324 (2016).

[14] A. Higginson, R. J. Gray, M. King, R. J. Dance, S. D. R. Williamson, N. M. H. Butler, R. Wilson, R. Capdessus, C. Armstrong, J. S. Green, et al., Nature Comm. **9**, 724 (2018).

[15] R. A. Snavely, M. H. Key, S. P. Hatchett, T. E. Cowan, M. Roth, T. W. Phillips, M. A. Stoyer, E. A. Henry, T. C. Sangster, M. S. Singh, S. C. Wilks, A. MacKinnon, A. Offenberger, D. M. Pennington, K. Yasuike, A. B. Langdon, B. F. Lasinski, J. Johnson, M. D. Perry, and E. M. Campbell, Phys. Rev. Lett. **85**, 14 (2000)

[16] A. Maksimchuk, S. Gu, K. Flippo, and D. Umstadter, and V. Yu. Bychenkov, Phys. Rev. Lett. **84**, 18 (2000)

[17] S. C. Wilks, A. B. Langdon, T. E. Cowan, M. Roth, M. Singh, S. Hatchett, M. H. Key, D. Pennington, A. MacKinnon, and R. A. Snavely, Phys. Plasmas **8**, 542 (2001).

[18] J. Fuchs, P. Antici, E. D'Humieres, E. Lefebvre, M. Borghesi, E. Brambrink, C. A. Cecchetti, M. Kaluza, V. Malka, and M. Manclossi, Nature Physics **2**, 48 (2006)

[19] T. Esirkepov, M. Borghesi, S. V. Bulanov, G. Mourou, and T. Tajima, Phys. Rev. Lett. **92**, 175003 (2004).

[20] A. Henig, S. Steinke, M. Schnürer, T. Sokollik,3 R. Hörlein, D. Kiefer, D. Jung, J. Schreiber, B. M. Hegelich, X. Q. Yan, J. Meyer-ter-Vehn, T. Tajima, P. V. Nickles, W. Sandner, and D. Habs, Phys. Rev. Lett. **103**, 245003 (2009)

[21] J. H. Bin, W. J. Ma, H. Y. Wang, M. J. V. Streeter, C. Kreuzer, D. Kiefer, M. Yeung, S. Cousens, P. S. Foster, B. Dromey, X. Q. Yan,3 R. Ramis, J. Meyer-ter-Vehn, M. Zepf, and J. Schreiber, Phys. Rev. Lett. **115**, 064801 (2015)

[22] D. Haberberger, S. Tochitsky, F. Fiuza, C. Gong, R. A. Fonseca, L. O. Silva, W. B. Mori, and C. Joshi, Nature Physics **8**, 95 (2012)

[23] S. Palaniyappan, B. M. Hegelich, H.-C. Wu, D. Jung, D. C. Gautier, L. Yin, B. J. Albright, R. P. Johnson, T. Shimada, S. Letzring, D. T. Offermann, J. Ren, C. Huang, R. Horlein, B. Dromey, J. C. Fernandez, and R. C. Shah, Nature Physics **8**, 763 (2012).

[24] A. V. Kuznetsov, T. Zh. Esirkepov, F. F. Kamenets, and S. V. Bulanov, Plasma Phys. Rep. **27**, 211 (2001); S. V. Bulanov and T. Zh. Esirkepov, Phys. Rev. Lett. **98**, 049503 (2007).

[25] S. S. Bulanov,E. Esarey,C. B. Schroeder, S. V. Bulanov, T. Zh. Esirkepov, M. Kando, F. Pegoraro, W. P. Leemans, Phys. Plasmas **23**, 056703 (2016).

[26] L. Willingale, S. P. D. Mangles, P. M. Nilson, R. J. Clarke, A. E. Dangor, M. C. Kaluza, S. Karsch, K. L. Lancaster, W. B. Mori, Z. Najmudin, J. Schreiber, A. G. R. Thomas, M. S. Wei, and K. Krushelnick, Phys. Rev. Lett. **96**, 245002 (2006).

[27] Y. Fukuda, A. Ya. Faenov, M, Tampo, T. A. Pikuz, T. Nakamura, H. Kando, Y. Hayashi, A. Yogo, H. Sakaki, T. Kameshima, A. S. Pirozhkov, K. Ogura, M. Mori, T. Zh. Esirkepov, J. Koga, A. S. Boldarev, V. A. Gasilov, A. I. Magunov, Y. Yamauchi, R. Kodama, P. R. Bolton, Y. Kato, T. Tajima, H. Daido, and S. V. Bulanov, Phys. Rev. Lett. **103**, 165002 (2009).

[28] L. Willingale, P. M. Nilson, A. G. R. Thomas, S. S. Bulanov, A. Maksimchuk, W. Nazarov, T. C. Sangster, C. Stoeck, and K. Krushelnick, Phys. Plasmas **18**, 056706 (2011).

[29] M. H. Helle, D. F. Gordon, D. Kaganovich, Y. Chen, J. P. Palastro, and A. Ting, Phys. Rev. Lett. **117**, 165001 (2016).

[30] S. S. Bulanov, V. Y. Bychenkov, V. Chvykov, G. Kalinchenko, D. William L., T. Matsuoka, A. G. R. Thomas, L. Willingale, V. Yanovsky, K. Krushelnick, and A. Maksimchuk Phys of Plasmas **17**, 043105 (2010)

[31] T. Nakamura, S. V. Bulanov, T. Z. Esirkepov, and M. Kando PRL **105** 135002 (2010)

[32] S. S. Bulanov, E. Esarey, C. B. Schroeder, W. P. Leemans, S. V. Bulanov, D. Margarone, G. Korn, and T. Haberer, Phys. Rev. Special Topics - Accelerators and Beams **18**, 061302 (2015)

[33] A. Sharma and A. Andreev, Laser and Particle Beams **34** 219 (2016)

[34] A. Sharma, Scientific Reports **8** 2191 (2018)

[35] S. S. Bulanov, E. Esarey, C. B. Schroeder, S. V. Bulanov, T. Zh. Esirkepov, M. Kando, F. Pegoraro, and W. P. Leemans, Phys. Rev. Lett. **114**, 105003 (2015).

[36] C. S. Brady, C. P. Ridgers, T. D. Arber, and A. R. Bell, Plasma Phys. Control. Fusion **55**, 124016 (2013).

[37] X. L. Zhu, T. P. Yu, Z. M. Sheng, Y. Yin, I. C. E. Turcu, and A. Pukhov, Nature Communications 7, 13686 (2016).

[38] J.-x. Liu, Y. Zhao, X.-p. Wang, J.-z. Quan, T.-p. Yu, G.-B. Zhang, X.-h. Yang, Y.-y. Ma, F.-q. Shao, and J. Zhao, Physics of Plasmas **25**, 103106 (2018).

[39] Y.-J. Gu, O. Klimo, S. V. Bulanov, and S. Weber, Communications Physics **1**, 93 (2018)

[40] P. Chen, J. J. Su, T. Katsouleas, S. Wilks, and J. M. Dawson, IEEE Trans. Plasma Sci. **15**, 218 (1987).

[41] Guo-Zheng Sun, Edward Ott, Y. C. Lee, and Parvez Guzdar, Phys. Fluids **30** 2 (1987)

[42] D. J. Stark, T. Toncian, and A. V. Arefiev, Phys. Rev. Lett. **116**, 185003 (2016);

[43] O. Jansen, T. Wang, D. Stark, E. d'Humieres, T. Toncian, and A. Arefiev, Plasma Phys. Cointrol. Fusion **60**, 054006 (2018)

[44] A. V. Arefiev, Z. Gong, T. Toncian, and S. S. Bulanov, arXiv:1807.07629

[45] J.-L. Vay, A. Almgren, J. Bell, L. Ge, D.P. Grote, M. Hogan, O. Kononenko, R. Lehe, A. Myers, C. Ng, J. Park, R. Ryne, O. Shapoval, M. Thvenet, and W. Zhang, Nuclear Inst. and Methods in Physics Research, A 01.035 (2018)

[46] O. Shapoval, J.-L. Vay, H. Vincenti, Comp. Phys. Comm. (2018)

[47] S. Steinke, J. H. Bin, J. Park, Q. Ji, K. Nakamura, A. J. Gonsalves, S. S. Bulanov, C. Toth, J-L. Vay, C. B. Schroeder, E. Esarey, T. Schenkel, and W. P. Leemans, submitted to Physical Rev. A (2019)